Modelling the behaviour of steel fibre reinforced concrete using a discrete strong discontinuity approach

C. Octávio[a], D. Dias-da-Costa[b,c], J. Alfaiate[a], E. Júlio[a]

[a] *CEris, ICIST, Dept. Civil Eng., Instituto Superior Técnico, Universidade de Lisboa, Av. Rovisco Pais 1049–001 Lisboa, Portugal*
[b] *School of Civil Engineering, The University of Sydney, NSW2006, Australia*
[c] *ISISE, Dept. Civil Eng., University of Coimbra, Rua Luís Reis Santos, 3030–788 Coimbra, Portugal*

Abstract

The use of Fibre Reinforced Concrete (FRC) is gradually wide-spreading due to the significant advantages relatively to Normal Concrete (NC). In the case of steel fibres, the quasi-brittle behaviour of plain concrete structures can be modified into an enhanced ductile behaviour as a direct result of this addition. Since the mechanical properties of both FRC and NC can be significantly different, this work aims at developing a finite element formulation to specifically address the simulation of the behaviour of FRC members up to failure. For this purpose, the Conforming Generalised Strong Discontinuity Approach (CGSDA) is adopted with steel fibres explicitly introduced in the finite element mesh. The resulting formulation has the following main characteristics: *i*) variational consistency; *ii*) fibre elements automatically considered regardless of the presence of cracks; and *iii)* no additional degrees of freedom are required. The proposed formulation is validated using experimental results from tests conducted with different dosages of steel fibres.

Keywords: Strong embedded discontinuity, Discrete crack approach, Fibre reinforced concrete

Nomenclature

$\mathbf{a}$	total displacement vector at the nodes
$\hat{\mathbf{a}}$	regular displacement vector at the nodes
$\tilde{\mathbf{a}}$	enhanced displacement vector at the nodes
$\bar{\mathbf{b}}$	body forces vector
$\mathbf{B}$	strain-nodal displacement matrix
$\mathbf{B}_w$	enhanced strain-nodal displacement matrix
$\mathbf{D}$	constitutive matrix
E	Young's modulus
$\hat{\mathbf{f}}$	vector force at the regular nodes
f_c	compressive strength
f_t	tensile strength
$\mathbf{f}_w$	vector force at the additional nodes
G_F	fracture energy
h	parameter defining the jump transmission to Ω^+ and Ω^-
$\mathbf{H}_{\Gamma_d}$	diagonal matrix containing the Heaviside function evaluated at each degree of freedom
$\mathcal{H}_{\Gamma_d}$	Heaviside function
i, j	nodes placed at both extremities of the discontinuity
$\mathbf{I}$	identity matrix
k, l	nodes placed at both extremities of the fibres
k_n, k_s	normal and shear penalty parameters, respectively
$\mathbf{K}_{aa}$	bulk stiffness matrix

$\mathbf{K}_{aw}$, $\mathbf{K}_{wa}$, $\mathbf{K}_{ww}$ enhanced bulk stiffness matrices

$\mathbf{K}_d$ discontinuity stiffness matrix

l_d discontinuity length

$\mathbf{L}$ differential operator matrix

$\mathbf{M}_{R_w}$ matrix transmitting the rigid body motion from the discontinuity opening

$\mathbf{M}_{nR_w}$ matrix transmitting the non–rigid body motion from the discontinuity opening

$\mathbf{M}_w$ matrix transmitting the displacement resulting from the discontinuity opening

$\mathbf{M}_w^{k^*}$ matrix containing the contribution of the discontinuities of all enriched elements to each node of the element

$\mathbf{n}$ unit vector normal to the boundary

$\mathbf{N}$ shape function matrix

$\mathbf{n}^+$ unit vector normal to the discontinuity surface

$\mathbf{N}_w$ enhanced shape function matrix

n_{el} number of enriched elements

$\mathbb{N}$ enhanced fibre shape function matrix

P external load

$\mathbf{t}$ traction vector

$\bar{\mathbf{t}}$ natural forces vector

$\mathbf{T}$ discontinuity constitutive matrix

$\mathbf{u}$ total displacement vector

$\hat{\mathbf{u}}$ regular displacement field vector

$\tilde{\mathbf{u}}$ enhanced displacement field vector

$[\![\mathbf{u}]\!]$ jump vector

$\mathbf{w}^*$ nodal jump vector

$\mathbf{x}$ global coordinates of a material point

$\mathbf{x}_1, \mathbf{x}_2$ global frame

α_d discontinuity angle

$\boldsymbol{\beta}$ diagonal matrix of the contribution of each enriched element

Γ boundary

Γ_d discontinuity surface

Γ_t boundary with natural forces

Γ_u boundary with essential conditions

$\boldsymbol{\varepsilon}$ total strain tensor

$\boldsymbol{\sigma}$ stress tensors

ν Poisson ratio

Ω body

$d(\cdot)$ incremental variation of $(\cdot)$

$(\cdot)^s$ symmetric part of $(\cdot)$

$\delta(\cdot)$ admissible or virtual variation of $(\cdot)$

δ_{Γ_d} Dirac's delta–function along the surface Γ_d

$(\cdot)^e$ $(\cdot)$ belonging to the finite element e

$(\cdot)^f$ $(\cdot)$ belonging to the fibre element f

$(\cdot)^+$, $(\cdot)^-$ $(\cdot)$ at the positive and negative side of the discontinuity, respectively

$(\cdot)_n$, $(\cdot)_s$ normal and shear component of $(\cdot)$

1. Introduction

Fibre Reinforced Concrete (FRC) has several advantages when compared to Normal Concrete (NC). The presence of steel fibres enables crack bridging and a post-cracking tensile strength, which delays the development of classic failure mechanisms. When compared to the classic quasi-brittle behaviour of plain concrete structures, the FRC provides an enhanced response with improved ductility.

In recent years, a significant number of experimental studies related with FRC has been carried out. There are, however, still few numerical approaches capable of simulating the behaviour with the discrete representation of fracture and fibres. In terms of the modelling of the discontinuity, three main strategies can be found for FRC: (i) lattice models, e.g. [1–4]; (ii) smeared crack models, e.g. [5–8]; and (iii) the discrete crack approach, e.g. [9–11]. Lattice models [1–4], by their nature, automatically simulate the fibres as if it were discrete elements, and without the need to increase the total degrees of freedom of the system. Nevertheless, there are still difficulties in the application of such models, namely those related with the definition of material properties and geometry of the elements used to model the bulk.

Existing smeared models have differences in what concerns the simulation of fibres. The approaches proposed by Peng and Meyer [5] and by Caner *et al.* [8], for instance, do not explicitly simulate the fibres in the bulk, being these only taken into account for cracked finite elements. Peng and Meyer [5] assumed the fibres to decrease damage in the parent elements, whereas Caner *et al.* [8] used a reference strain given by the average opening of all cracks, within a certain length, to activate the fibres. Radtke *et al.* [6] simulated the fibres by means of equivalent loads applied at the nodes of parent elements. In this case, a micro-mechanical model provides the force needed to pull-out the fibres from the cementitious matrix, being the pull-out distance given by the opening of the crack bridged by the fibre. Also within the scope of the smeared crack approach, Cunha *et al.* [7] provided an approach to embed discrete fibres in the finite element mesh using constitutive pull-out laws from experimental tests. A common limitation underlying smeared models lies on the fact that the simulation of cracks not being discrete. As a consequence, specific regularisation techniques are required to avoid mesh dependency issues and true material separation might be very difficult to simulate.

Discrete crack models have been used by different authors. Denneman *et al.* [9] modelled fracture using an embedded discontinuity approach, although with the discrete simulation of the fibres. Wu *et al.* [12] defined cracks using local degrees of freedom at element level, in which case jumps and traction forces are not

continuous along the cracks and the stiffness of the fibre is not directly taken into account. A different approach, based on zero-thickness interface elements [13] was presented by Caggiano *et al.* [10] and Etse *et al.* [11] to simulate the fracture of bulk elements. The mixture theory [14] was used in this case to account for the fibre-concrete interaction, reason why the fibres were not explicitly simulated as discrete embedded elements.

Having all the above works under consideration, a different approach is herein followed for modelling FRC with discrete representation of cracks and fracture. The approach is developed within the scope of the discrete crack approach and has the following features:

i) fibres simulated as discrete elements embedded in the finite element mesh, both in pre-cracking and post-cracking stages;
ii) cracking handled by means of a discrete crack approach, which avoids mesh dependency and the need for regularisation techniques;
iii) the number of degrees of freedom of the problem unchanged and independent of the number of fibres.

In this scope, a discrete conforming formulation introduced in [15] is adopted for the simulation of crack propagation. This formulation is built at element level, following the embedment concept, and presents the following main advantages: *i*) variational consistency; *ii*) no limitations on the choice of the parent finite element; *iii*) comprehensive kinematics of the discontinuity, including both rigid body motion and stretching; *iv*) fully compatible enhanced kinematic field; *v*) additional global degrees of freedom located at the discontinuity; *vi*) continuity of both jumps and tractions across element boundaries; and *vii*) stress locking free. The strategy adopted to embed fibres within the finite element mesh is described in the following main sections.

The outline of the manuscript is as follows: first the kinematics of a strong discontinuity and the variational formulation are reviewed in Section 2; the element technology issues are presented in Section 3, whereas in Section 4, a structural example is presented and discussed for validation purposes; finally, in Section 5, the main conclusions are drawn.

2. General framework

The discrete crack approach framework is herein adopted for the description of discontinuities within a body. According to this, microcracking is assumed to develop as soon as the tensile strength of the material is reached. Microcracking then localises in a zero width surface of discontinuity, Γ_d, which follows a

stress-jump softening relation. Due to the traction continuity condition, the bulk gradually unloads during this softening process. The onset of localisation is identified using an initiation criterion, selected before the analysis [16]. In this case, a simple Mode-I opening, i.e., the Rankine criterion [17–20] is adopted.

2.1. Kinematics of a strong discontinuity

In this section the kinematics of a strong discontinuity is briefly presented. For that purpose, consider the body Ω illustrated in Fig. 1, where Γ represents the external boundary and Γ_d the internal boundary related with the discontinuity, the latter defining two subregions: Ω^+ and Ω^-. All loading is assumed to be quasi-statically applied and includes body forces, $\bar{\mathbf{b}}$, and both natural and essential boundary conditions, $\bar{\mathbf{t}}$ and $\bar{\mathbf{u}}$, respectively applied on external boundaries Γ_t and Γ_u. Vector $\mathbf{n}$ is defined orthogonally to the boundary surface and pointing outwards, whereas $\mathbf{n}^+$ is orthogonal to the discontinuity and pointing inwards Ω^+.

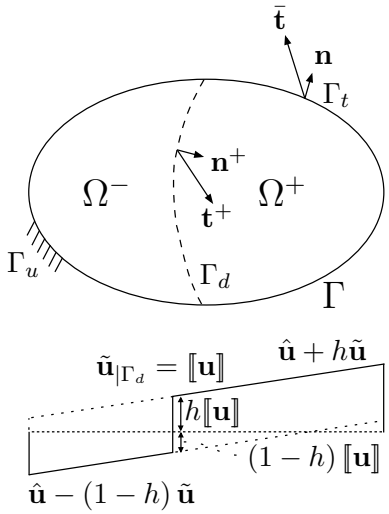

Figure 1: Domain Ω crossed by a strong discontinuity Γ_d and 1-D representation of the displacement field.

The displacement field inside the body, $\mathbf{u}$, has two different parts: *i*) the regular displacement field, $\hat{\mathbf{u}}$; and *ii*) the enhanced displacement field, $\tilde{\mathbf{u}}$, the latter exclusively due to the discontinuity opening, such that:

$$\mathbf{u}(\mathbf{x}) = \hat{\mathbf{u}}(\mathbf{x}) + \mathcal{H}_{\Gamma_d}\tilde{\mathbf{u}}(\mathbf{x}), \tag{1}$$

where $\mathcal{H}_{\Gamma_d}$ stands for the standard Heaviside function.

According to Fig. 1, the jump at the discontinuity, $[\![\mathbf{u}]\!]$, is obtained by applying Eq. (1) to both sides:

$$[\![\mathbf{u}]\!] = \left(\mathbf{u}^{+} - \mathbf{u}^{-}\right)_{|\Gamma_d} = \tilde{\mathbf{u}}_{|\Gamma_d}. \tag{2}$$

In the case of small displacements, the strain field is given by the following equation:

$$\boldsymbol{\varepsilon} = \boldsymbol{\nabla}^{\mathrm{s}}\mathbf{u} = \boldsymbol{\nabla}^{\mathrm{s}}\hat{\mathbf{u}} + \mathcal{H}_{\Gamma_d}\boldsymbol{\nabla}^{\mathrm{s}}\tilde{\mathbf{u}} + \delta_{\Gamma_d}\left([\![\mathbf{u}]\!] \otimes \mathbf{n}^{+}\right)^{\mathrm{s}} \text{ at } \Omega, \tag{3}$$

where $(\cdot)^{\mathrm{s}}$ corresponds to the symmetric part of $(\cdot)$ and $\otimes$ to the dyadic product.

2.2. Variational formulation

The principle of virtual work for the problem under consideration can be written as [15, 21–23]:

$$-\int_{\Omega\setminus\Gamma_d} (\boldsymbol{\nabla}^{\mathrm{s}}\delta\mathbf{u}) : \boldsymbol{\sigma}(\boldsymbol{\varepsilon})\, d\Omega - \int_{\Gamma_d} \delta[\![\mathbf{u}]\!] \cdot \mathbf{t}^{+}\, d\Gamma + \int_{\Omega\setminus\Gamma_d} \delta\mathbf{u}\cdot\bar{\mathbf{b}}\, d\Omega + \int_{\Gamma_t} \delta\mathbf{u}\cdot\bar{\mathbf{t}}\, d\Gamma = 0, \tag{4}$$

which is the classic principle of virtual work with an additional term representing the work at the discontinuity.

3. Element technology

This section presents the discretised set of equations developed for finite elements with embedded discontinuities and fibres.

3.1. Element interpolation

A body Ω is now discretised into finite elements. Fig. 2 represents one of those elements, with domain Ω^e, that contains one discontinuity Γ_d^e and one fibre Γ_f^e. The discontinuity is assumed to be straight and cross an entire finite element and is defined by two nodes, i and j, placed on the edges of the enriched finite element. The fibre is also straight and defined using two tip nodes, k and l, which can sit anywhere inside the finite element or at its edges. If the fibre spans across more than one finite element, the fibre is simply discretised and handled at element level. It is highlighted that the nodes used to define the fibre are fictitious and, therefore, do not give rise to additional degrees of freedom.

According to [15], the displacement field due to a strong discontinuity, given in Eq. (1), can be approximated using the following equations:

$$\mathbf{u}^e = \mathbf{N}^e(\mathbf{x})\left[\mathbf{a}^e + \left(\mathcal{H}_{\Gamma_d}\mathbf{I} - \mathbf{H}_{\Gamma_d}\right)\tilde{\mathbf{a}}^e\right] \quad \text{if } \mathbf{x} \in \Omega^e \setminus \Gamma_d^e, \tag{5}$$

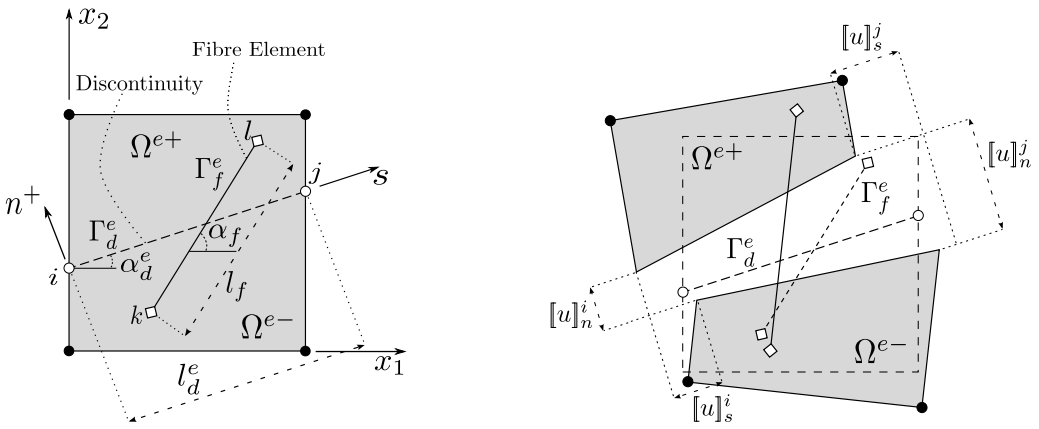

Figure 2: Domain Ω^e crossed by a strong discontinuity Γ_d^e and a fibre Γ_f^e: (a) definitions; and (b) general opening.

$$[\![\mathbf{u}]\!]^e = \mathbf{u}^{e+} - \mathbf{u}^{e-} = \mathbf{N}^e(\mathbf{x})\,\tilde{\mathbf{a}}^e \quad \text{at } \Gamma_d^e, \tag{6}$$

where $\mathbf{N}^e$ contains the element shape functions, $\mathbf{a}^e$ are the total nodal degrees of freedom related to $\mathbf{u}^e$, $\tilde{\mathbf{a}}^e$ are the enhanced nodal degrees of freedom related to $\tilde{\mathbf{u}}^e$ and $\mathbf{H}_{\Gamma_d}$ is a diagonal matrix with '1' for nodal degrees of freedom belonging to Ω^{e+} and '0' otherwise.

The displacement for an embedded fibre element is interpolated using the following equation:

$$\mathbf{u}^f = \mathbf{N}^f \mathbf{a}^f \quad \text{at } \Gamma_f^e, \tag{7}$$

where $\mathbf{N}^f$ are shape functions of a truss element and $\mathbf{a}^f$ are the total nodal degrees of freedom corresponding to nodes 'k' and 'l'. Since these degrees of freedom can be obtained using Eq. (5), the following equation can be written:

$$\mathbf{u}^f = \mathbb{N}^f(\mathbf{x}) \left[\mathbf{I}^f \mathbf{a}^e + \mathbf{H}_{\Gamma_d}^f \tilde{\mathbf{a}}^e \right] \quad \text{at } \Gamma_f^e, \tag{8}$$

where $\mathbb{N}^f$ is defined by:

$$\mathbb{N}^f(\mathbf{x}) = \mathbf{N}^f(\mathbf{x}) \begin{bmatrix} \mathbf{N}^e(\mathbf{x}_k) & \mathbf{0} \\ \mathbf{0} & \mathbf{N}^e(\mathbf{x}_l) \end{bmatrix}, \tag{9}$$

and $\mathbf{I}^f$ and $\mathbf{H}_{\Gamma_d}^f$ are obtained by staking into rows the identity matrix and $(\mathcal{H}_{\Gamma_d}\mathbf{I} - \mathbf{H}_{\Gamma_d})$, respectively, evaluated at each node of the fibre.

The strain field is derived by applying the standard differential operator $\mathbf{L}$ to Eqs. (5) and (8), respectively leading to:

$$\boldsymbol{\varepsilon}^e = \underbrace{\mathbf{L}^e \mathbf{N}^e(\mathbf{x})}_{\mathbf{B}^e(\mathbf{x})} \left[\mathbf{a}^e + \left(\mathcal{H}_{\Gamma_d}\mathbf{I} - \mathbf{H}_{\Gamma_d}\right)\tilde{\mathbf{a}}^e\right] \text{ in } \Omega^e \setminus \Gamma_d^e \tag{10}$$

and

$$\boldsymbol{\varepsilon}^f = \underbrace{\mathbf{L}^f \mathbb{N}^f(\mathbf{x})}_{\mathbf{B}^f(\mathbf{x})} \left[\mathbf{I}^f \mathbf{a}^e + \mathbf{H}^f_{\Gamma_d}\tilde{\mathbf{a}}^e\right] \text{ at } \Gamma_f^e. \tag{11}$$

The corresponding incremental stress is derived from:

$$d\boldsymbol{\sigma}^e = \mathbf{D}^e \mathbf{B}^e(\mathbf{x}) \left[d\mathbf{a}^e + \left(\mathcal{H}_{\Gamma_d}\mathbf{I} - \mathbf{H}_{\Gamma_d}\right) d\tilde{\mathbf{a}}^e\right] \text{ in } \Omega^e \setminus \Gamma_d^e, \tag{12}$$

$$d\boldsymbol{\sigma}^f = \mathbf{D}^f \mathbf{B}^f(\mathbf{x}) \left[\mathbf{I}^f d\mathbf{a}^e + \mathbf{H}^f_{\Gamma_d} d\tilde{\mathbf{a}}^e\right] \text{ at } \Gamma_f^e, \tag{13}$$

whereas the incremental traction at the discontinuity is obtained from Eq. (6) as:

$$d\mathbf{t}^e = \mathbf{T}^e d[\![\mathbf{u}]\!]^e = \mathbf{T}^e \mathbf{N}^e(\mathbf{x})\, \tilde{\mathbf{a}}^e \text{ at } \Gamma_d^e. \tag{14}$$

In Eqs. (12) to (14), $\mathbf{D}^e$, $\mathbf{D}^f$ and $\mathbf{T}^e$ are the tangent stiffness matrices of the bulk, fibre element and discontinuity, respectively.

3.2. General kinematics

In this section, a detailed description of the enhanced displacement field is provided. Further discussion on this topic can be found in [15, 22–24]. The following derivations are obtained using the CGSDA [15]. Accordingly, the enhanced nodal degrees of freedom can be written as follows:

$$\tilde{\mathbf{a}}^e = \mathbf{M}_w^{ek^*} \mathbf{w}^{e^*}, \tag{15}$$

where $\mathbf{w}^{e*}$ is a vector containing the additional degrees of freedom due to the discontinuity from all n_{el} enriched neighbouring elements, and matrix $\mathbf{M}_w^{ek*}$ acts as a means of transmitting the opening of the discontinuity to the regular nodes of the finite element. Matrix $\mathbf{M}_w^{ek*}$ has the contribution of all enriched neighbouring elements, such that each row $\mathbf{M}_w^{ei*}$ corresponds to the i-node of the element, and is given by:

$$\mathbf{M}_w^{ei^*} = \mathbf{M}_w^e + \sum_{j=1, j\neq e}^{n_{el}} \boldsymbol{\beta}^j \left\{\mathbf{M}_w^j - \mathbf{M}_w^e\right\}, \tag{16}$$

where $\boldsymbol{\beta}^j$ is a diagonal matrix for each node, containing $\beta^j_{x_i}$ terms for both directions (x_1, x_2), computed by:

$$\beta^j_{x_i} = \frac{K^j_{i,x_i}}{\sum_{k=1}^{n_{el}} K^k_{i,x_i}}. \tag{17}$$

In Eqs. (16) and (17), K^j_{i,x_i} is the stiffness matrix component of the bulk for element j, direction x_i. $\mathbf{M}^e_w$ is the matrix transmitting both rigid and stretching opening modes of Ω^{e+} over Ω^{e-} [23], defined as:

$$\mathbf{M}^e_w = \mathbf{M}^e_{Rw} + \mathbf{M}^e_{nRw}, \tag{18}$$

with

$$\mathbf{M}^e_{R_w} = \begin{bmatrix} 1 - \frac{(x_2 - x_2^i)\sin\alpha^e_d}{l^e_d} & \frac{(x_2 - x_2^i)\cos\alpha^e_d}{l^e_d} & \frac{(x_2 - x_2^i)\sin\alpha^e_d}{l^e_d} & -\frac{(x_2 - x_2^i)\cos\alpha^e_d}{l^e_d} \\ \frac{(x_1 - x_1^i)\sin\alpha^e_d}{l^e_d} & 1 - \frac{(x_1 - x_1^i)\cos\alpha^e_d}{l^e_d} & -\frac{(x_1 - x_1^i)\sin\alpha^e_d}{l^e_d} & \frac{(x_1 - x_1^i)\cos\alpha^e_d}{l^e_d} \end{bmatrix}, \tag{19}$$

$$\mathbf{M}^e_{nR_w} = \begin{bmatrix} -\frac{s^e_n[1+\cos(2\alpha^e_d)]}{2} & -\frac{s^e_n[\sin(2\alpha^e_d)]}{2} & \frac{s^e_n[1+\cos(2\alpha^e_d)]}{2} & \frac{s^e_n[\sin(2\alpha^e_d)]}{2} \\ -\frac{s^e_n[\sin(2\alpha^e_d)]}{2} & -\frac{s^e_n[1-\cos(2\alpha^e_d)]}{2} & \frac{s^e_n[\sin(2\alpha^e_d)]}{2} & \frac{s^e_n[1-\cos(2\alpha^e_d)]}{2} \end{bmatrix} \tag{20}$$

and

$$s^e_n = \frac{s(\mathbf{x})}{l^e_d} = (x_1 - x_1^i)\frac{\cos\alpha^e_d}{l^e_d} + (x_2 - x_2^i)\frac{\sin\alpha^e_d}{l^e_d}, \tag{21}$$

where $\mathbf{x} = (x_1, x_2)$ is the global position of any material point inside the bulk, (x_1^i, x_2^i) is the global position of crack tip i, whilst l^e_d and α^e_d are the length and angle defining the discontinuity (see Fig. 2a).

3.3. Discretised equations

Eq. (15) can now be introduced in Eqs. (1), (6), (8) and (12) to (14), and then used to discretise Eq. (4). By progressively taking: *i)* $\delta d\mathbf{w}^{e*} = 0$; and *ii)* $\delta d\mathbf{a}^e = 0$, the following system is derived:

$$\left(\mathbf{K}^e_{aa} + \mathbf{K}^f_{aa}\right) d\mathbf{a}^e - \left(\mathbf{K}^e_{aw} + \mathbf{K}^f_{aw}\right) d\mathbf{w}^{e^*} = d\mathbf{f}^e, \tag{22}$$

$$-\left(\mathbf{K}^e_{wa} + \mathbf{K}^f_{wa}\right) d\mathbf{a}^e + \left(\mathbf{K}^e_{ww} + \mathbf{K}^e_d + \mathbf{K}^f_{ww}\right) d\mathbf{w}^{e^*} = d\mathbf{f}^e_w, \tag{23}$$

where $\mathbf{K}^e_{aa} = \int_{\Omega^e \setminus \Gamma^e_d} \mathbf{B}^{eT} \mathbf{D}^e \mathbf{B}^e \, d\Omega^e$, $\mathbf{K}^e_{aw} = \int_{\Omega^e \setminus \Gamma^e_d} \mathbf{B}^{eT} \mathbf{D}^e \mathbf{B}^e_w \, d\Omega^e$, $\mathbf{K}^e_{wa} = \int_{\Omega^e \setminus \Gamma^e_d} \mathbf{B}^{eT}_w \mathbf{D}^e \mathbf{B}^e \, d\Omega^e$, $\mathbf{K}^e_{ww} = \int_{\Omega^e \setminus \Gamma^e_d} \mathbf{B}^{eT}_w \mathbf{D}^e \mathbf{B}^e_w \, d\Omega^e$, $\mathbf{K}^e_d = \int_{\Gamma^e_d} \mathbf{N}^{eT}_w \mathbf{T}^e \mathbf{N}^e_w \, d\Gamma^e$, $\mathbf{K}^f_{aa} = \int_{\Gamma_f} \mathbf{B}^{fT} \mathbf{D}^f \mathbf{B}^f \, A^f d\Gamma_f$, $\mathbf{K}^f_{wa} = \int_{\Gamma_f} \mathbf{B}^{fT}_w \mathbf{D}^f \mathbf{B}^f \, A^f d\Gamma_f$, $\mathbf{K}^f_{ww} = \int_{\Gamma_f} \mathbf{B}^{fT}_w \mathbf{D}^f \mathbf{B}^f_w \, A^f d\Gamma_f$, and

$$\mathbf{B}^e_w = \mathbf{B}^e (\mathcal{H}_{\Gamma_d} \mathbf{I} - \mathbf{H}_{\Gamma_d}) \mathbf{M}^{ek*}_w, \tag{24}$$

$$\mathbf{B}^f_w = \mathbf{B}^f \left(\mathbf{I}^f \mathbf{a}^e + \mathbf{H}^f_{\Gamma_d} \tilde{\mathbf{a}}^e \right) \mathbf{M}^{ek*}_w, \tag{25}$$

$$\mathbf{N}^e_w = \mathbf{N}^e (\mathcal{H}_{\Gamma_d} \mathbf{I} - \mathbf{H}_{\Gamma_d}) \mathbf{M}^{ek*}_w \tag{26}$$

and A^f is the area of the fibre.

The external forces are computed using the following equations, where the self-weight of the fibre has been omitted:

$$d\mathbf{f}^e = \int_{\Omega^e \setminus \Gamma^e_d} \mathbf{N}^{eT} \bar{\mathbf{b}}^e \, d\Omega^e + \int_{\Gamma^e_t} \mathbf{N}^{eT} \bar{\mathbf{t}}^e \, d\Gamma^e, \tag{27}$$

$$d\mathbf{f}^e_w = \int_{\Omega^e \setminus \Gamma^e_d} \mathbf{N}^{eT}_w \bar{\mathbf{b}}^e \, d\Omega^e + \int_{\Gamma^e_t} \mathbf{N}^{eT}_w \bar{\mathbf{t}}^e \, d\Gamma^e. \tag{28}$$

Since this formulation is variationally consistent, symmetry is kept in the case of symmetric constitutive laws.

3.4. Implementation issues

The distribution of fibres is herein considered to be a random process. The coordinates of one of the tips of the fibre and corresponding angle are randomly generated. After this step, the coordinates of the second tip of the fibre are directly calculated using its length and angle. Only fibres generated inside the specimen are considered valid. This process is carried out until reaching the pre-defined dosage of fibres. Since the process of enrichment is exclusively built at element level, whenever a fibre spans across more than one finite element, the fibre is discretised into segments defined by the intersections with the edges of the bulk elements.

In the case of elements not cracked, the system of Eqs. (22) and (23) is simplified by deleting all terms related with $d\mathbf{w}^{e*}$. The onset of crack localisation is identified using a *non-local* stress state adopted in the vicinity of the crack tip

[15, 25]. The algorithm used for crack propagation and to enforce path continuity is detailed in [15]. The degrees of freedom of the additional nodes due to cracking are global, thus jump and traction are continuous along the crack path [24].

4. Case study

The proposed formulation is herein applied to the simulation of experimental results from Costa *et al.* [26]. The experiment consists on a three-point bending beam and different dosages of steel fibres. The experimental set-up and corresponding results are summarised in Section 4.1, whereas the numerical simulations are discussed in Section 4.2.

4.1. Three point FRC bending beam

The experimental set-up is presented in Fig. 3a, and a typical failure mechanism obtained during the tests is shown in Fig. 3b.

(a) (b)

Figure 3: Three point FRC bending beam: (a) test set-up; and (b) failure mechanism during a test.

The specimen is a $850 \times 100 \times 100\,\text{mm}^3$ prism with a $20 \times 50 \times 100\,\text{mm}^3$ mid-span notch at the bottom. Costa *et al.* [26] tested three different dosages of steel fibres (0.25%, 0.50% and 1.00%), with two beams for each dosage, as well as two reference beams without steel fibres. In Fig. 4, the load vs. mid-span vertical displacement curves are presented for the tested specimens. From this figure it can be concluded that the gradual increase of fibres leads to the modification of the structural behaviour. For lower dosages the response is similar to a non-reinforced concrete specimen, whereas for higher dosages the response becomes more ductile, with an increased peak load.

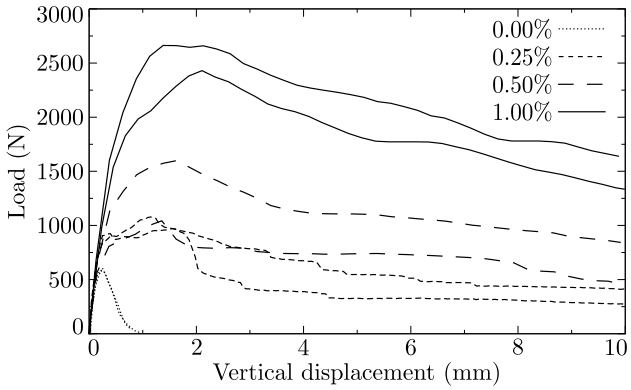

Figure 4: Three point FRC bending beam: experimental results for all specimens from [26].

According to Fig. 4, there is a significant difference between the two 0.50% specimen responses. Unfortunately, the specimen with the lower peak load was not properly produced in laboratory, which resulted in a different fibre distribution (see Fig. 5). For this reason, this curve is not included in the analyses described in the following section.

4.2. Numerical simulations

In Fig. 6a the structural scheme adopted for the numerical simulation is presented. The following concrete parameters were experimentally determined by Costa *et al.* [26] for the mixture without fibres: Young's modulus $E_c = 24500$ N/mm^2; compressive strength $f_c = 59.1$ N/mm^2; tensile strength $f_{t0} = 2.0$ N/mm^2; fracture energy $G_F = 0.05$ N/mm; and Poisson's ratio $\nu = 0.2$. After localisation, the discontinuity is assumed to follow a mode-I fracture exponential constitutive law.

The properties of the fibres are the following: diameter $d_f = 0.375$ mm; Young's modulus $E_f = 200000$ N/mm^2; and Poisson's ratio $\nu = 0.3$. The constitutive law includes the bond behaviour between steel fibres according with the guidelines found in Model Code 2010 [27]. The law was obtained after a preliminary numerical study using the specimens with 0.25% of fibres (see Fig. 7). The fibres were then randomly distributed, as detailed in Section 3.4, considering ten different distributions for each fibre dosage.

The mesh is composed of 901 bilinear elements and 4225 fibre elements in the area of the notch, as shown in Fig. 6b for one of the three 0.25% models. The number of fibres increases for the following two cases, reaching 8450 and 16900 fibre elements for 0.50% and 1.00%, respectively.

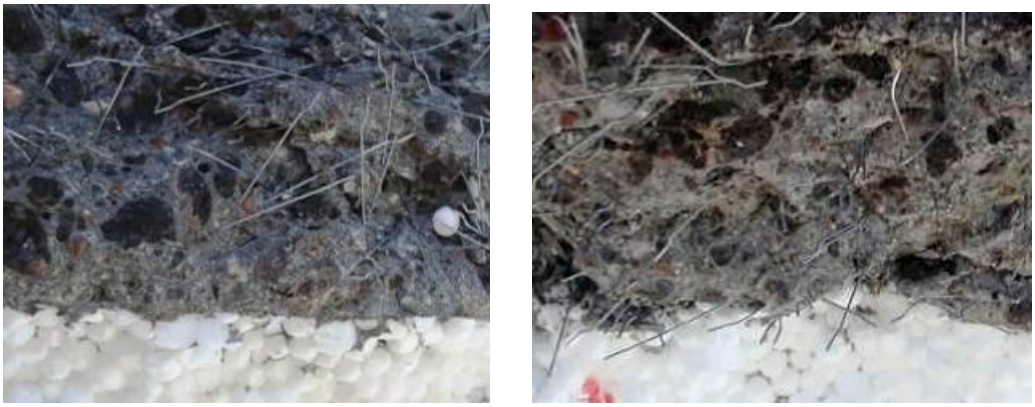

(a) (b)

Figure 5: Three point FRC bending beam: fibre distribution on top of the notch for the specimens with 0.50% of steel fibres: (a) wrong distribution in one specimen; and (b) adequate distribution according to [26].

The arc-length method is used to enforce the monotonic growth of the normal opening of the notch. Results shown in Figs. 8 to 10 reveal a similar crack path among all models and dosages of steel fibres, which is in agreement with the experimental observation. In Fig. 8 the crack path for one of the models with 0.50% of steel fibres is shown as example, with the fibres being omitted for clarity purposes.

Comparison between experimental [26] and numerical results is shown in Fig. 9, where the envelope for the ten considered distributions is shown in grey. There is good agreement between experimental and numerical models, with similar initial stiffness, peak load and post-peak ductile behaviour (see Table 1).

	Peak load (N)			Fracture energy (N/mm)		
	0.25%	0.50%	1.00%	0.25%	0.50%	1.00%
Exp. (Spec. 1)	951.0	1566.0	2472.0	0.8813	2.1738	4.2588
Exp. (Spec. 2)	1062.0	-	2691.0	1.2285	-	3.6471
Exp. (Average)	1006.5	1566.0	2581.5	1.0549	2.1738	3.9530
Num. (Average)	901.5	1470.4	2673.9	1.1009	2.0215	3.8246
|Error|	10.43%	6.11%	3.58%	4.36%	7.01%	3.25%

Table 1: Comparison between the experimental and numerical results, in terms of peak load and fracture energy.

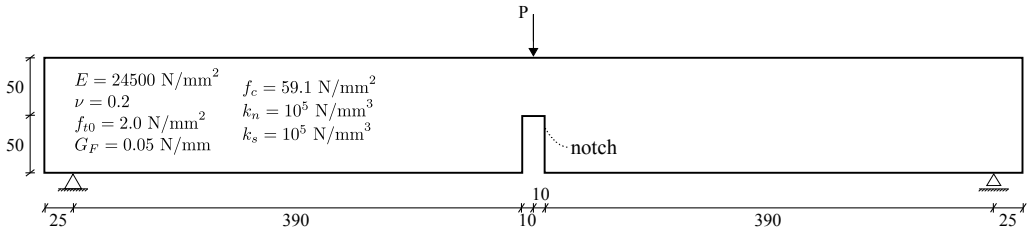

(a)

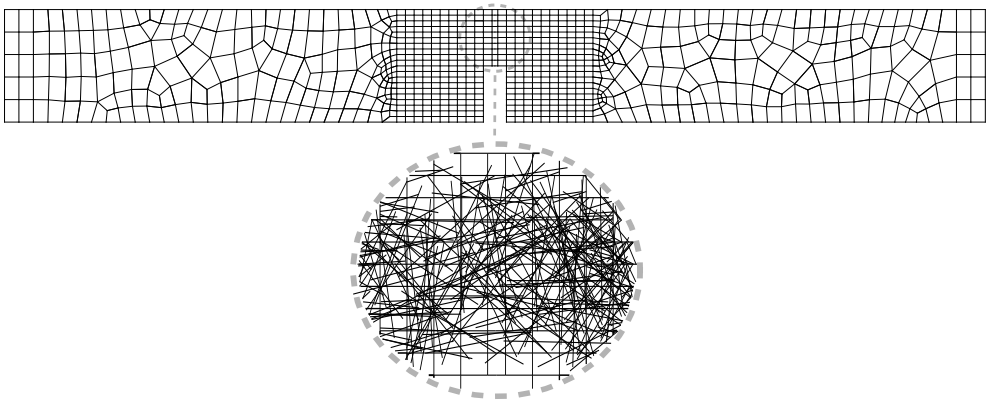

(b)

Figure 6: Three point FRC bending beam: (a) structural scheme (100 mm width, dimensions in mm); and (b) mesh adopted for one of the 0.25% models, showing a detail near the notch for one of the three fibre distributions considered.

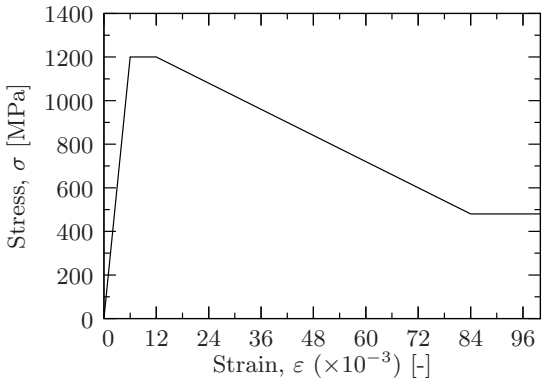

Figure 7: Three point FRC bending beam: adopted constitutive law for the steel fibres.

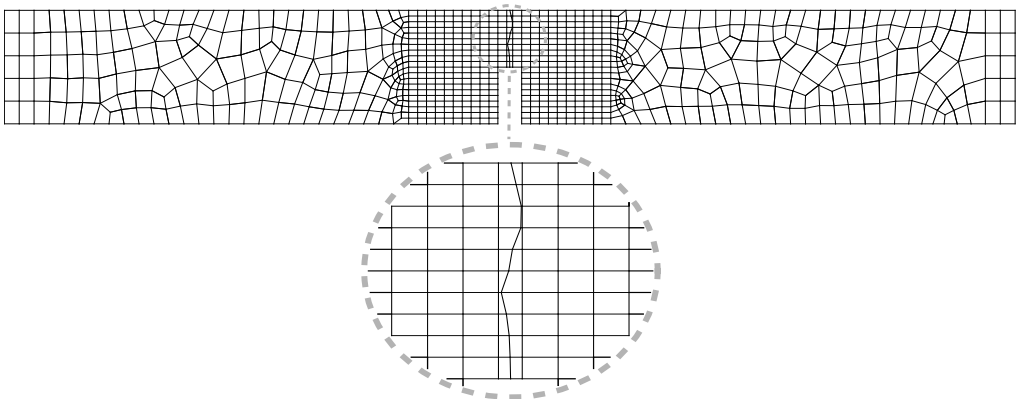

Figure 8: Three point FRC bending beam: crack path for a steel fibres dosage of 0.50%

Table 1 contains experimental and numerical results concerning the peak load and fracture energy, the latter computed according to [28]. The error is generally significantly below 10%, which denotes the good agreement of the numerical model for all fibre dosages, regardless of the experimental variability expected in this type of material.

In Fig. 10, the deformed mesh is shown with the corresponding principal stress maps for three different stages with the steel fibre dosage of 0.50%. It is interesting to note that the tensile bulb developing at the crack front gradually spreads across larger areas with increasing fibre dosage, showing the bridging effect on the propagating crack (see the details in Fig. 11). In all cases, the obtained stresses are always below the tensile strength.

Observing Fig. 10 it is possible to conclude that the proposed formulation

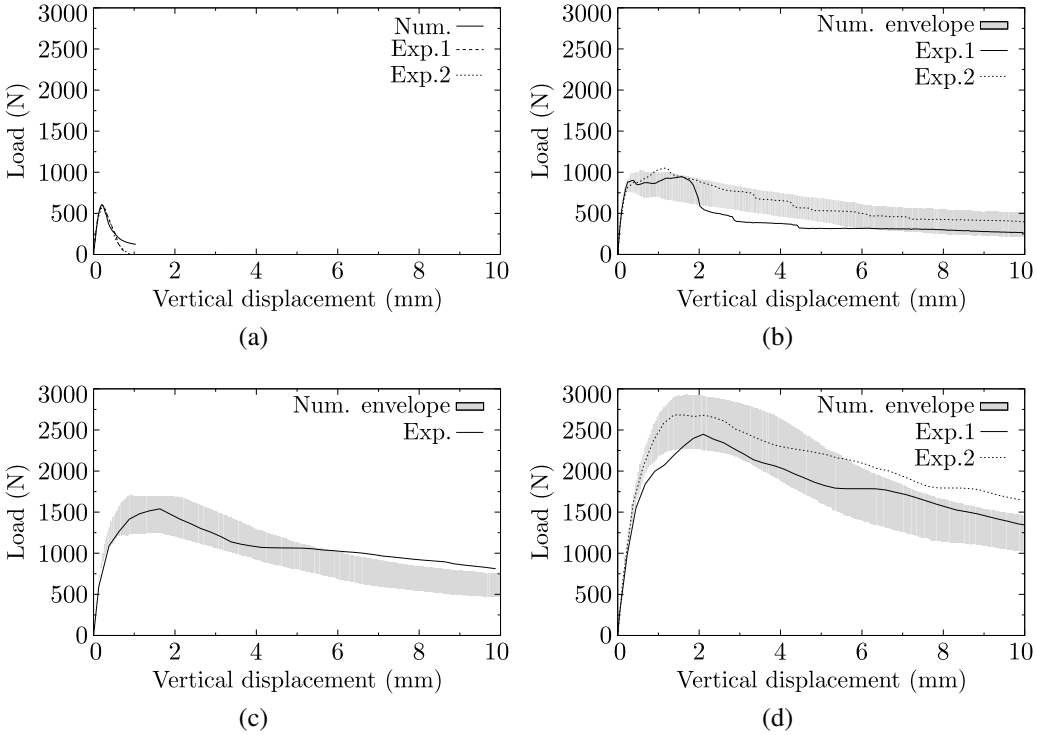

Figure 9: Three point FRC bending beam: load vs. mid-span vertical displacement curves for steel fibres dosages of: (a) 0.00%; (b) 0.25%; (c) 0.50%; and (d) 1.00%

reproduces the stress field in the bulk, with the stresses gradually approaching zero in the vicinity of the crack due to the debonding of steel fibres. Higher stresses are visible in Figs. 10a and 10b in the central region of the specimen. These peak values represent the bridging effect, which increases with the number of fibres crossing the crack. It should be highlighted that these peak stresses are smaller than the tensile strength for all tested dosages of fibres.

5. Conclusions

In this paper a new formulation was presented for the simulation of the behaviour of FRC structures. The innovative features include the discrete simulation of both cracks and steel fibres, which are embedded into finite elements. Thus, the formulation is entirely built at element level and remains variationally consistent. Due to the discrete crack approach framework adopted, relatively coarse meshes

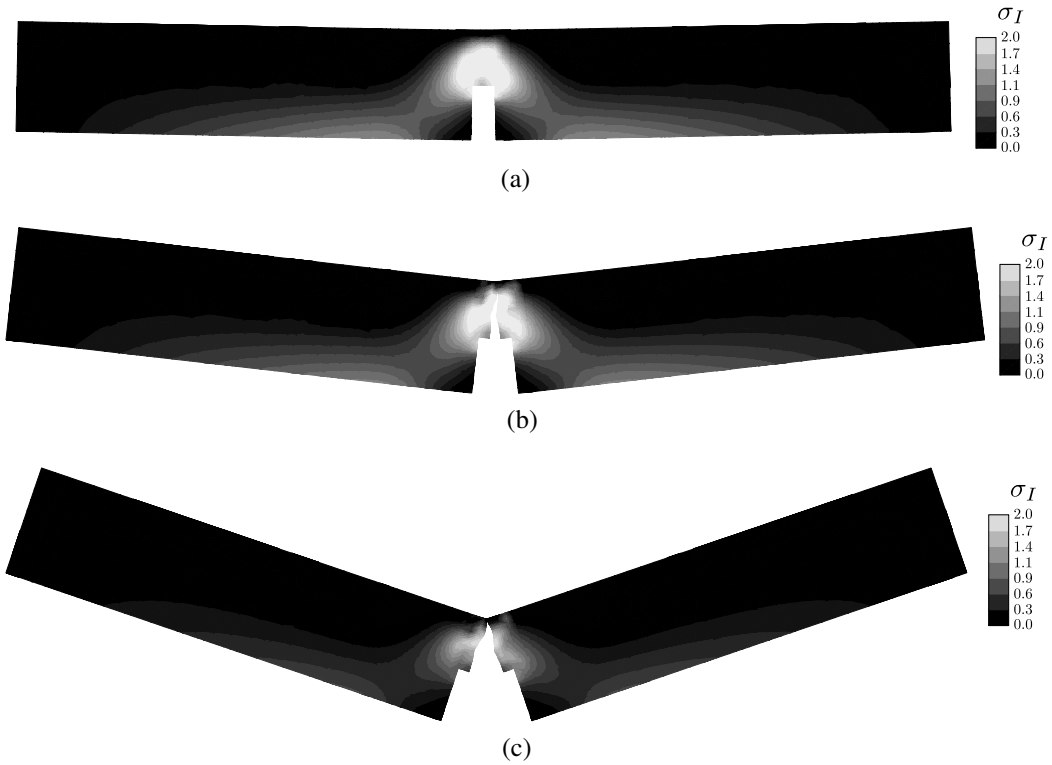

Figure 10: Three point FRC bending beam: σ_1 (N/mm^2) map obtained for: (a) $\delta_v = 0.5$ mm; (b) $\delta_v = 3.0$ mm; and (c) $\delta_v = 9.0$ mm (displacements magnified 15 times).

can be used without the need for special regularisation techniques. It is highlighted that: *i*) no additional degrees of freedom are required to embed the fibre elements; and *ii*) the fibre elements are considered during pre and post-cracking stages. Bond between fibre and cementitious material is considered implicitly by adopting a constitutive law derived from the Model Code 2010 [27].

The formulation was validated in the simulation of three-point FRC bending beams. It is emphasised the good agreement between crack paths and load vs. displacement curves, for all studied dosages of steel fibres. The model adequately captures the initial stiffness of the experimental specimens during the pre-cracking stage. Afterwards, both peak load and post-peak ductile behaviour are in accordance with the experimental observations for increasing dosages of steel fibres. The model shows the development of the tensile bulb surrounding the crack tip front, which results from the bridging effect responsible for delaying the propagation and softening of the tensile stress at the crack. This increases the ductility of the

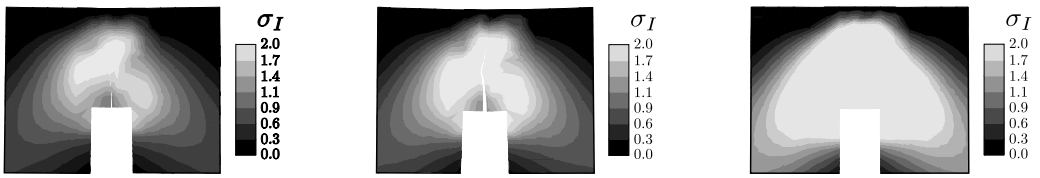

Figure 11: Principal stresses details at the specimen mid-span for the considered steel fibres dosages: (a) 0.25%; (b) 0.50%; and (c) 1.00%

structural member. These results are quite promising and the authors will continue developing this models towards the simulation of the distributed cracking forming inside the tensile bulb for higher dosages of fibres. The possibility of introducing the slippage of the fibres will also be addressed.

6. Acknowledgements

This work is supported by FEDER funds through the Operational Programme for Competitiveness Factors – COMPETE – and by Portuguese funds through FCT – Portuguese Foundation for Science and Technology under Project No. FCOMP-01-0124-FEDER-020275 (FCT ref. PTDC/ECM/119214/2010) and Ph.D. Grant SFRH/BD/85922/2012. The second author would also like to acknowledge the Funding support from the Australian Research Council through project DE150101703.

References

[1] J. E. Bolander, S. Saito, Discrete modelling of short-fibre reinforcement in cementitious composites, Advanced Cement Based Materials 6 (3-4) (1997) 76–86, doi: 10.1016/s1065-7355(97)90014-6.

[2] J. E. Bolander, S. Choi, S. R. Duddukuri, Fracture of fiber-reinforced cement composites: effects of fiber dispersion, International Journal of Fracture 154 (1-2) (2008) 73–86, doi: 10.1007/s10704-008-9269-4.

[3] M. Kunieda, H. Ogura, N. Ueda, H. Nakamura, Tensile fracture process of strain hardening cementitious composites by means of three-dimensional meso-scale analysis, Cement and Concrete Composites 33 (9) (2011) 956–965, doi: 10.1016/j.cemconcomp.2011.05.010.

[4] J. Kang, J. E. Bolander, Simulating crack width distributions in SHCC under tensile loading, in: G. Ruiz, C. Andrade, J. G. M. van Mier, R. C. Yu (Eds.), VIII International Conference on Fracture Mechanics of Concrete and Concrete Structures, FraMCoS-8, Toledo, Spain, 2013.

[5] X. Peng, C. Meyer, A continuum damage mechanics model for concrete reinforced with randomly distributed short fibers, Computers and Structures 78 (5) (2000) 505–515, doi: 10.1016/s0045-7949(00)00045-6.

[6] F. K. F. Radtke, A. Simone, L. J. Sluys, A computational model for failure analysis of fibre reinforced concrete with discrete treatment of fibres, Engineering Fracture Mechanics 77 (4) (2010) 597–620, doi: 10.1016/j.engfracmech.2009.11.014.

[7] V. Cunha, J. Barros, J. Sena Cruz, A finite element model with discrete embedded elements for fibre reinforced composites, Computers and Structures 94-95 (0) (2012) 22–33, doi: 10.1016/j.compstruc.2011.12.005.

[8] F. C. Caner, Z. P. Bažant, R. Wendner, Microplane model m7f for fiber reinforced concrete, Engineering Fracture Mechanics 105 (0) (2013) 41–57, doi: 10.1016/j.engfracmech.2013.03.029.

[9] E. Denneman, R. Wu, E. Kearsley, A. Visser, Discrete fracture in high performance fibre reinforced concrete materials, Engineering Fracture Mechanics 78 (10) (2011) 2235–2245, doi: 10.1016/j.engfracmech.2011.04.008.

[10] A. Caggiano, G. Etse, E. Martinelli, Zero-thickness interface model formulation for failure behavior of fiber-reinforced cementitious composites, Computers and Structures 98-99 (0) (2012) 23–32, doi: 10.1016/j.compstruc.2012.01.013.

[11] G. Etse, A. Caggiano, S. Vrech, Multiscale failure analysis of fiber reinforced concrete based on a discrete crack model, International Journal of Fracture 176 (1-2) (2012) 131–146, doi: 10.1007/s10704-012-9733-z.

[12] R. Wu, E. Denneman, J. T. Harvey, Evaluation of embedded discontinuity method for finite element analysis of cracking of hot-mix asphalt concrete, Transportation Research Record 2127 (1) (2009) 82–89, doi: 10.3141/2127-10.

[13] I. Carol, P. Prat, C. López, Normal/shear cracking model: Application to discrete crack analysis, Journal of Engineering Mechanics 123 (8) (1997) 765–773, doi: 10.1061/(ASCE)0733-9399(1997)123:8(765).

[14] C. Truesdell, R. Toupin, The classical field theories, in: S. Flgge (Ed.), Principles of Classical Mechanics and Field Theory / Prinzipien der Klassischen Mechanik und Feldtheorie, Vol. III / I of Encyclopedia of Physics / Handbuch der Physik, Springer Berlin Heidelberg, 1960, pp. 226–858, doi: 10.1007/978-3-642-45943-6_2.

[15] D. Dias-da-Costa, J. Alfaiate, L. J. Sluys, P. Areias, E. Júlio, An embedded formulation with conforming finite elements to capture strong discontinuities, International Journal for Numerical Methods in Engineering 93 (2) (2013) 224–244, doi: 10.1002/nme.4393.

[16] J. Alfaiate, G. N. Wells, L. J. Sluys, On the use of embedded discontinuity elements with crack path continuity for mode-i and mixed-mode fracture, Engineering Fracture Mechanics 69 (6) (2002) 661–686, doi: 10.1016/S0013-7944(01)00108-4.

[17] E. Schlangen, Experimental and numerical analysis of fracture processes in concrete, Ph.D. thesis, Delft University of Technology (1993).

[18] J. C. Galvez, M. Elices, G. V. Guinea, J. Planas, Mixed mode fracture of concrete under proportional and nonproportional loading, International Journal of Fracture 94 (3) (1998) 267–284, doi: 10.1023/A:1007578814070.

[19] F. Barpi, S. Valente, Numerical simulation of prenotched gravity dam models, Journal of Engineering Mechanics 126 (6) (2000) 611–619, doi: 10.1061/(ASCE)0733-9399(2000)126:6(611).

[20] J. C. Galvez, J. Cervenka, D. A. Cendón, V. Saouma, A discrete crack approach to normal/shear cracking of concrete, Cement and Concrete Research 32 (10) (2002) 1567–1585, doi: 10.1016/S0008-8846(02)00825-6.

[21] L. E. Malvern, Introduction to the mechanics of a continuous medium, Prentice-Hall International, Englewood Cliffs, New Jersey, 1969.

[22] D. Dias-da-Costa, J. Alfaiate, L. J. Sluys, E. Júlio, A discrete strong discontinuity approach, Engineering Fracture Mechanics 76 (9) (2009) 1176–1201, doi: 10.1016/j.engfracmech.2009.01.011.

[23] D. Dias-da-Costa, J. Alfaiate, L. J. Sluys, E. Júlio, Towards a generalization of a discrete strong discontinuity approach, Computer Methods in Applied Mechanics and Engineering 198 (47-48) (2009) 3670–3681, doi: 10.1016/j.cma.2009.07.013.

[24] J. Alfaiate, A. Simone, L. J. Sluys, Non-homogeneous displacement jumps in strong embedded discontinuities, International Journal of Solids and Structures 40 (21) (2003) 5799–5817, doi: 10.1016/S0020-7683(03)00372-x.

[25] G. N. Wells, L. J. Sluys, A new method for modelling cohesive cracks using finite elements, International Journal for Numerical Methods in Engineering 50 (12) (2001) 2667–2682, doi: 10.1002/nme.143.

[26] H. Costa, D. Esteves, E. Júlio, T. Simões, Design and characterization of self-compacting fibre-reinforced lightweight aggregate concrete, in: J. Barros (Ed.), 8th RILEM International Symposium on Fibre Reinforced Concrete, BEFIB2012, Guimarães, Portugal, 2012.

[27] *fib*, Model Code for Concrete Structures 2010 – Final draft, Volume 1. *fib Bulletin* 65 (2012).

[28] F. Bencardino, L. Rizzuti, G. Spadea, R. Swamy, Experimental evaluation of fiber reinforced concrete fracture properties, Composites Part B: Engineering 41 (1) (2010) 17 – 24, doi: 10.1016/j.compositesb.2009.09.002.